JGR Oceans

RESEARCH ARTICLE
10.1029/2023JC019914

The Occurrence, Variability, and Potential Drivers of Submesoscale Eddies in the Southern California Bight Based on a Decade of High-Frequency Radar Observations

A. R. Payandeh[1], L. Washburn[1], B. Emery[1], and J. C. Ohlmann[2]

[1]Marine Science Institute, University of California, Santa Barbara, Santa Barbara, CA, USA, [2]Earth Research Institute, University of California, Santa Barbara, Santa Barbara, CA, USA

Key Points:

- Recurring submesoscale eddies form hotspots of eddy activity, largely in association with topographical features
- Submesoscale eddy counts increased by 40% in association with the 2014–2015 marine heatwave and the 2015–2016 El Niño
- The formation of submesoscale eddies displayed a domain-wide diurnal cycle with the diurnal winds as the potential underlying mechanism

Correspondence to:
A. R. Payandeh,
alip@ucsb.edu

Citation:
Payandeh, A. R., Washburn, L., Emery, B., & Ohlmann, J. C. (2023). The occurrence, variability, and potential drivers of submesoscale eddies in the Southern California Bight based on a decade of high-frequency radar observations. *Journal of Geophysical Research: Oceans*, *128*, e2023JC019914. https://doi.org/10.1029/2023JC019914

Received 9 APR 2023
Accepted 25 SEP 2023

Abstract Submesoscale eddies form an important component of the circulation of the Southern California Bight (SCB). Despite their acknowledged significance in influencing ocean physics, biology, and ecological processes, submesoscale eddies have been exceptionally hard to study and observe because of the technical challenges posed by both field and remote platforms. Here, using a decade of high-frequency radar surface current observations, we describe submesoscale eddies in the SCB. Between 2012 and 2021, a total of ∼235,000 eddies were detected, averaging 452 ± 116 eddies per week. Recurring eddies in certain locations over time, formed hotspots of eddy activity, largely in association with topographical features. On seasonal scales, eddies were more numerous in the summer and early fall. At inter-annual scales, eddy counts increased by 40% in association with the 2014–2015 marine heatwave and the 2015–2016 El Niño. A domain-wide diurnal cycle was observed in the formation of eddies and the normalized vorticity. To determine the relative contributions of tides and diurnal winds, an analysis of spectral components and their spatial distribution along the SCB was conducted. The results revealed that while diurnal tides may exert some influence on the diurnal variations, their effect is comparatively minor when compared to diurnal winds. This conclusion was reached by considering the prevalence of the S_1 frequency, which is a meteorological tide known to be associated with motions induced by sea-land breeze. Overall, diurnal variability was more prominent in the southern SCB and less significant toward the north.

Plain Language Summary The Southern California Bight is abundant in submesoscale eddies, which are coherent rotating flow patterns with horizontal scales ranging from a few kilometers to tens of kilometers and temporal scales of a few hours to a few days. Over the last 10 years, a network of high-frequency radars, operating in this region has measured nearshore surface currents with high temporal and spatial resolution. Utilizing these data, we mapped the spatial distribution of submesoscale eddies, examined their seasonal and inter-annual variations, and analyzed their evolution. It was discovered that cyclonic (counterclockwise) eddies were more common than anticyclonic (clockwise) eddies. Recurring eddies formed hotspots of eddy activity, often linked to topographical features. Eddies were observed to be more frequent in the summer and fall compared to spring and winter, and their counts increased by 40% during the 2014–2015 marine heatwave and the 2015–2016 El Niño. Eddies were observed to form every 24 hr throughout the study domain. Further analysis revealed that the diurnal variability is primarily caused by sea-land breeze.

1. Introduction

Submesoscale eddies with spatial scales of a few kilometers to tens of kilometers are present everywhere in the global ocean and they are essential for the movement of nutrients, heat, momentum, and other waterborne materials (Lévy et al., 2012; Mahadevan, 2016; Munk et al., 2000). Submesoscale eddies are defined by horizontal scales less than the first baroclinic Rossby radius of deformation (20–30 km; Dong & McWilliams, 2007) and $O(1)$ Rossby and Richardson numbers (Mahadevan, 2016; McWilliams, 2016; Thomas et al., 2008). Observing submesoscale eddies using traditional observational platforms (e.g., boats, drifters, planes, gliders, and satellites) has proven challenging due to their small size and short lifetimes (Dauhajre et al., 2017; McWilliams, 2016; Y. Zhang et al., 2019). As a result, studies of submesoscale processes have benefited primarily from high-resolution numerical simulations (e.g., Capet et al., 2008; Dauhajre et al., 2017; Dong et al., 2009, 2012; Dong & McWilliams, 2007; Gula et al., 2015, 2016) and analytical models with idealized frameworks (e.g., Dauhajre & McWilliams, 2018; Mahadevan, 2006; Mahadevan & Tandon, 2006).

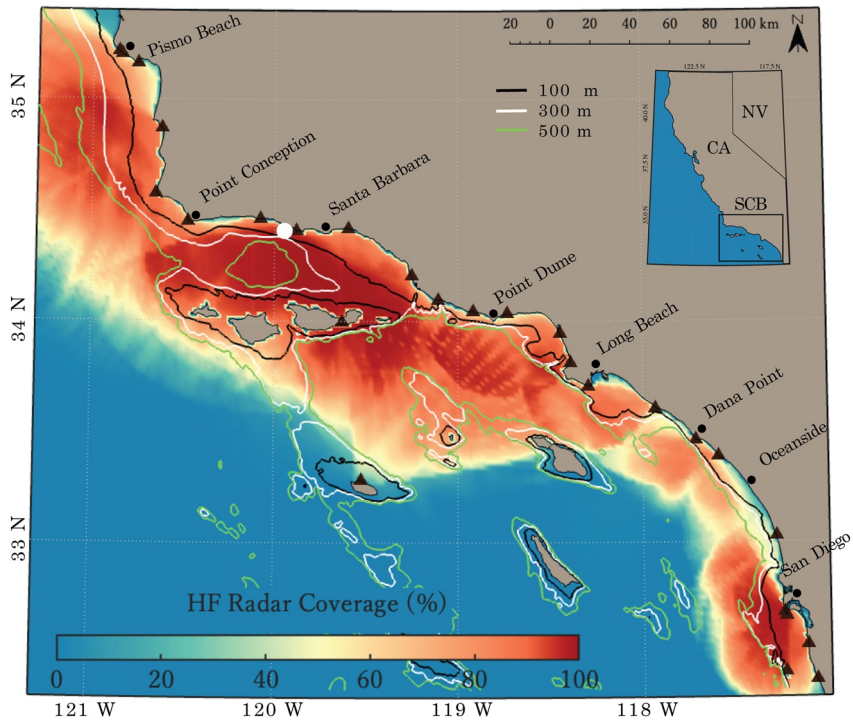

Figure 1. High-frequency radar (HFR) (2 km) temporal coverage during 2012–2021 in the Southern California Bight (SCB) as shown by the color bar. HFR sites (black triangles), and bathymetry (100 m black, 300 m white, and 500 m green), are also shown. The white circle indicates the Naples Reef Mooring, where 5-m temperature data were obtained.

Nevertheless, the expansion of high-frequency radar (HFR) networks worldwide and their increased application in circulation studies have demonstrated the capability of this technology to observe the complex submesoscale eddy field of the coastal ocean, especially in their upper range of length scales (5–20 km; Bassin et al., 2005; Kim, 2010; Kim et al., 2011; Kirincich, 2016; Kirincich & Lentz, 2017; Lai et al., 2017; Soh & Kim, 2018). Lai et al. (2017) used HFR observations to study submesoscales in the Taiwan Strait and found eddies ranging from 3 to 18 km. Kirincich (2016) did so for the Martha's Vineyard shelf using high-resolution (400 m) HFR observations and found 2–5 km eddies with lifetimes of less than 5 hr. Previous studies of multiyear records of HFR observations in the Southern California Bight (SCB; Figure 1) have focused on eddy characteristics. Kim (2010) analyzed a 2-year record of 1 km HFR data off San Diego, identifying submesoscale eddies with diameters of 5–15 km and lifetimes of 1–2 days. Soh and Kim (2018) used similar HFR observations and found that kinetic energy spectra off San Diego exhibit anisotropy associated with topographic features. In their study based on 6 km HFR observations nearly covering the US West coast, Kim et al. (2011) discovered that the most persistent submesoscale eddies are found in the Santa Barbara Channel (SBCh). Bassin et al. (2005) used HFR observations in the SBCh and found 4–15 km eddies with typical lifetimes of 2 days.

Previous modeling studies have shown that eddies in the SCB occur at spatial scales ranging from mesoscales to submesoscales. For example, numerical simulations by Dong et al. (2009) showed the occurrence of three persistent mesoscale eddies in the SCB, all cyclonic: one in the SBCh, the second in the central SCB, and the third to the southeast between Catalina and San Clemente Islands. Eddies with diameters ranging from 1 to 30 km were found around Santa Catalina Island by Caldeira et al. (2005) using ROMS. Dong et al. (2012) found that most eddies in the SCB are characterized as submesoscale, with an average radius of 5 km and most having radii less than 10 km in agreement with DiGiacomo and Holt (2001), who studied satellite SAR imagery spanning 1992–1998. They documented 107 eddies in the SCB, with 75% having diameters under 10 km and 94% under 20 km. They also found that over 90% of eddies were cyclonic.

Submesoscale eddies form an important component of the circulation of the SCB as they have a significant influence on ecological processes. Chenillat et al. (2015) discovered that eddies forming along the coast can act as a nutrient-trapping mechanism, leading to a sustained, locally enriched ecosystem over the lifetime of the eddy.

This isolated ecosystem within the eddy ultimately leads to a growth in planktonic productivity through Ekman pumping of nutrients. Brzezinski and Washburn (2011) found that cyclonic eddies in the western SBCh, enhance productivity through the retention of upwelled waters or eddy pumping or combinations of both mechanisms. Caldeira et al. (2005) found that islands in the SCB generated strong, localized wind curls and sheared currents that enhance nutrient enrichment around islands and were likely associated with strong vertical currents.

The dominant mechanisms responsible for the generation of submesoscale eddies include mixed layer instabilities, surface frontogenesis caused by mesoscale eddies, and topographic wakes (e.g., McWilliams, 2016; Thomas et al., 2008). In the SCB, the dominant mechanisms that generate eddies have been shown to be topographic current wakes and wind stress curls. For example, Dong et al. (2009) found that eddy kinetic energy distribution is strongly influenced by topography. Island wakes have been identified as a primary source of vorticity accounting for 30% of eddies (Caldeira et al., 2005; Dong & McWilliams, 2007; Marmorino et al., 2010). Based on the analysis of airborne SAR imagery, Marmorino et al. (2010) suggested that the formation of submesoscale eddies around Catalina Island is due to current-wake instability caused by the flow of the Southern California Countercurrent along the north shore of the island. The SCB is a unique area of the California Current System because it is not directly exposed to the strong equatorward winds that drive coastal circulation north of Point Conception (Hickey, 1993). Due to the bend in the coastline, the prevailing wind pattern has a positive curl that favors cyclonic eddies formation in the SBCh (Dong et al., 2009; Winant & Dorman, 1997).

Less is known about the seasonal and inter-annual variations of eddy activity in the SCB. High correlations between the wind stress curl and eddy kinetic energy levels on seasonal and longer time scales were found by Dong et al. (2009), who also noted a rise in eddy kinetic energy associated with the occurrence of the 1997 El Niño. El Niño's escalating influence on eddy activity has also been reported in other parts of the world (e.g., Chaigneau et al., 2008; Conejero et al., 2020; Espinoza-Morriberón et al., 2017). In addition to ENSO events, extreme warming events such as marine heatwaves (MHWs) have also been shown to affect eddy activity in the coastal ocean (Oliver et al., 2017). However, the effect of these climatic extremes on submesoscale activity in the SCB is still in question.

Since 2012, a network of HFRs has observed surface currents in the SCB. This record has captured significant, large-scale events on inter-annual timescales, including an unprecedented MHW (i.e., the "Blob," Bond et al., 2015) followed by a strong El Niño during 2015–2016. We utilized these data to investigate the spatial distribution, seasonal and inter-annual variability, and evolution of submesoscale eddies in the SCB.

2. Data and Methods

2.1. HFR Surface Currents

Hourly surface current measurements were collected from a network of 31 HFRs in the SCB and were computed on a 2-km grid. HFRs measure the velocity of the top ∼0.5–1 m of the ocean surface. Radars were operating at different transmitted frequencies near 13.6 and 25.6 MHz. Observed currents by HFRs are the average velocities from the surface to a depth of order $\lambda/4\pi$ where λ is the Bragg wavelength (Stewart & Joy, 1974). The difference in transmitted frequencies of radars used may result in a ∼42 cm difference in the effective depth of the radar measurement (0.88 m at 13.6 MHz and 0.46 at 25.6 MHz). The uncertainty of HFR surface current measurements has been estimated using ADCPs, and surface drifters in a number of studies and indicates errors of 6–15 cm s^{-1} (e.g., Emery et al., 2004; Emery & Washburn, 2019; Graber et al., 1997; Ohlmann et al., 2007; Paduan et al., 2006). Figure 1 shows the percentage of the time when data were available from January 2012 to December 2021. Generally, within 50 km of the coastline, data availability was high over most of the area with grid points having valid data greater than 85% of the time, with variation between 60% and 95%. HFR spatial coverage did not show significant monthly, seasonal, or inter-annual variations.

2.2. Eddy Detection

A vector geometry-based algorithm was applied for eddy detection (Nencioli et al., 2010). This method has been successfully applied in several previous studies (e.g., Dong et al., 2012; Pennelly & Myers, 2022; Zhao et al., 2021). In this method, four constraints must be met at a point to be detected as the center of an eddy. (a) The meridional velocity along the east-west axis must reverse direction and its magnitude must increase away from

the putative eddy center. (2) The same criteria must be met for the zonal velocity in the north-south direction. (c) Velocity must be locally minimum at the eddy center, and (d) a constant sense of rotation must occur around the center. This condition removes eddy-like features such as meanders. The algorithm uses two parameters: (a) parameter a, which defines the dimension (i.e., number of grid points) to search for velocity reversals and to check for a consistent sense of rotation around the eddy center, and (b) parameter b, which defines the dimension to search for local minima of velocity. A comparison between the eddies detected by the algorithm and those subjectively identified visually based on HFR current maps showed that using only one pair of parameters a and b underestimated the number of eddies. Therefore, a minor modification was applied to the algorithm to allow different pairs of a and b to be searched for velocity reversal and local velocity minima. Specifically, three pairs of a and b were employed, namely $a = 2$, $b = 2$; $a = 3$, $b = 3$; and $a = 4$, $b = 4$. Duplicate eddy centers resulting from these different a, b pairs were subsequently removed from the final results. As discussed in Section 3.1, these input configurations enabled the identification of eddies mostly within the submesoscale range (Figure 3). Eddy boundaries were identified as the outermost closed streamlines surrounding the center, where the velocity magnitudes continue to increase in the radial direction (Nencioli et al., 2010). Examples of identified eddies in various locations along the SCB are shown in Figure 2.

After detecting the eddy centers over 10 years of the study period, the eddy tracks are determined by comparing the centers at successive time steps, beginning from the initial time (t) when an eddy was first identified. The process of connecting the eddy tracks involves comparing the detected eddy centers at consecutive time steps. To establish eddy tracks, an eddy at time $t + 1$ is considered the same as the one identified at time t if they share the same type (cyclonic/anticyclonic) and if their centers are located within a radius (r) of 2 km around the center position at time t. In case no eddies are found within this radius at $t + 1$, a second search is conducted at $t + 2$ within an expanded area of $2r$ (4 km). If no eddies are detected at $t + 2$, it is considered that the eddy has dissipated, and the track is closed (Nencioli et al., 2010). The size of the search area strongly affects the accuracy of the eddy tracking. Due to the advection of eddies by local currents, a reasonable assumption to derive the searching radius is to multiply the average current speed (0.2 m s^{-1}) with the time step (1 hr), which gives the estimated displacement of 720 m. However, considering that the HFR grid points are spaced at 2 km intervals, a minimum searching area with a radius of $r = 2$ km should be sufficient for tracking eddies.

A key parameter of eddies is the rotation rate which is quantified here by the normalized vorticity ζ/f where $\zeta = \partial v/\partial x - \partial u/\partial y$ is relative vorticity and f is the Coriolis parameter. The first-order central difference was used to calculate the spatial derivatives of surface currents ($\partial v/\partial x$ and $\partial u/\partial y$).

2.3. Spectral Analysis

Identifying the dominant frequencies that exist in normalized vorticity and eddy formation allows for the potential driving mechanisms to be inferred, such as the barotropic tide or diurnal wind. Consequently, power spectra were calculated to analyze the periodicities present in both normalized vorticity and eddy formation. To analyze the alongshore variations, a line positioned 10 km from the shore and extending from the north to the south end of the study domain was selected, excluding the islands (red curve, Figure 11a). The power spectra were then computed at the grid points positioned along this line using the Welch method with a 50% overlap and applying a Hanning window (Welch, 1967). The length of data used for spectrum estimation may vary at each grid point due to changes in HFR coverage along this line. This variability is shown in Figure 12c. Overall, the 10-year HFR data provided a long enough record to accurately differentiate neighboring tidal frequencies such as K_1 and O_1, as well as S_2 and M_2. Moreover, the data length was even sufficient to distinguish closely spaced frequencies, such as K_1 (~0.0418 cph) and S_1 (~0.0417 cph).

3. Results and Discussion

3.1. Eddy Statistics

Using the Nencioli et al. (2010) method, we identified ~235,000 eddies within the footprint of hourly surface current maps from the HFR network, corresponding to 452 ± 116 eddies per week. This number includes repetitive counting of individual eddies through their lifetimes. The number of cyclonic eddies (56%) was greater than the number of anticyclonic eddies (44%). If eddies through their lifetimes are counted as one occurrence, the total number of eddy trajectories was ~100,000 (~192 trajectories per week) with roughly equal numbers of

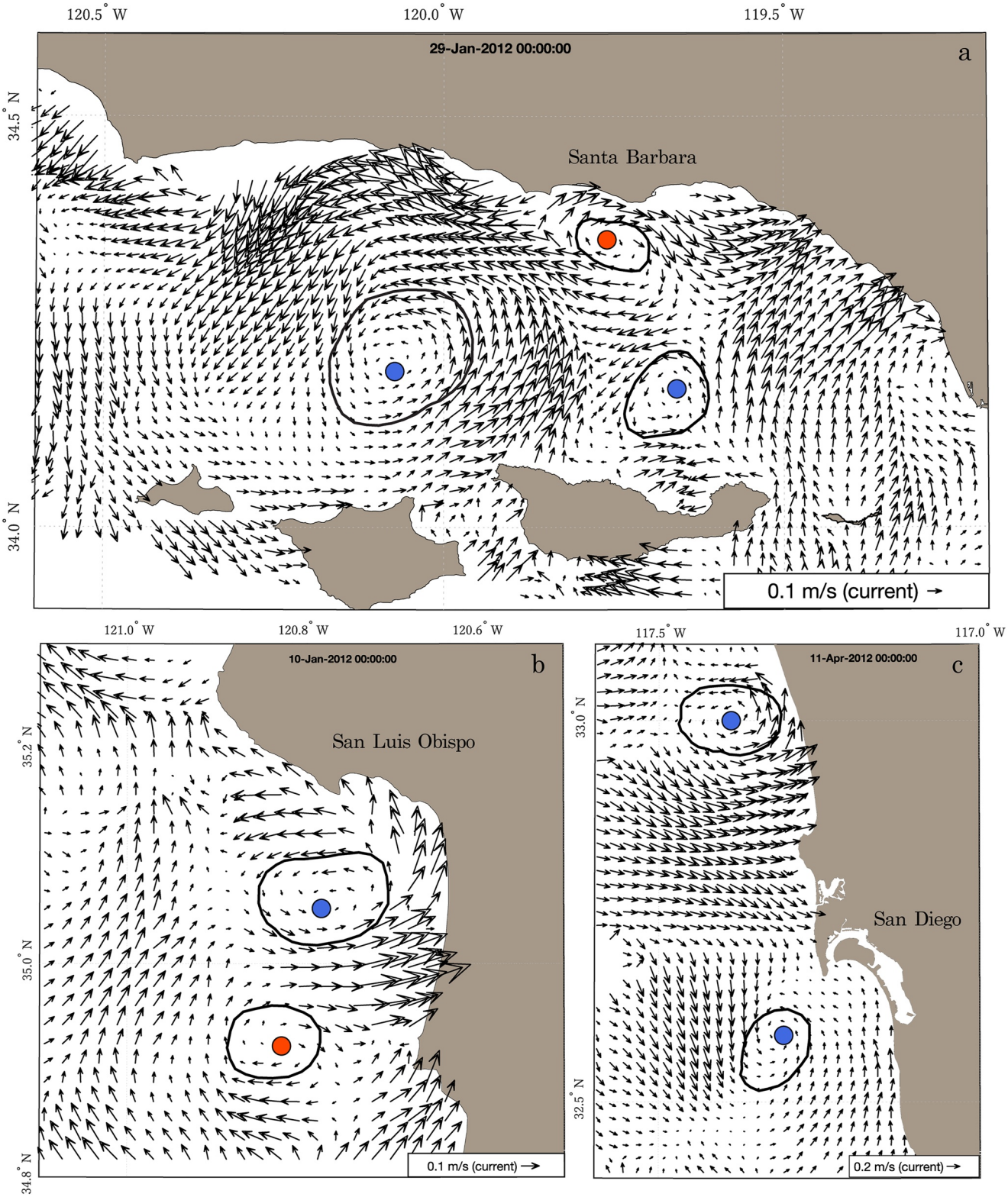

Figure 2. Examples of identified eddies in distinct locations: (a) the Santa Barbara Channel, (b) San Louis Obispo Bay, and (c) off San Diego. The detected eddy centers are represented by circles, with blue circles denoting cyclonic eddies and red circles representing anticyclonic eddies. The solid black lines indicate eddy boundaries.

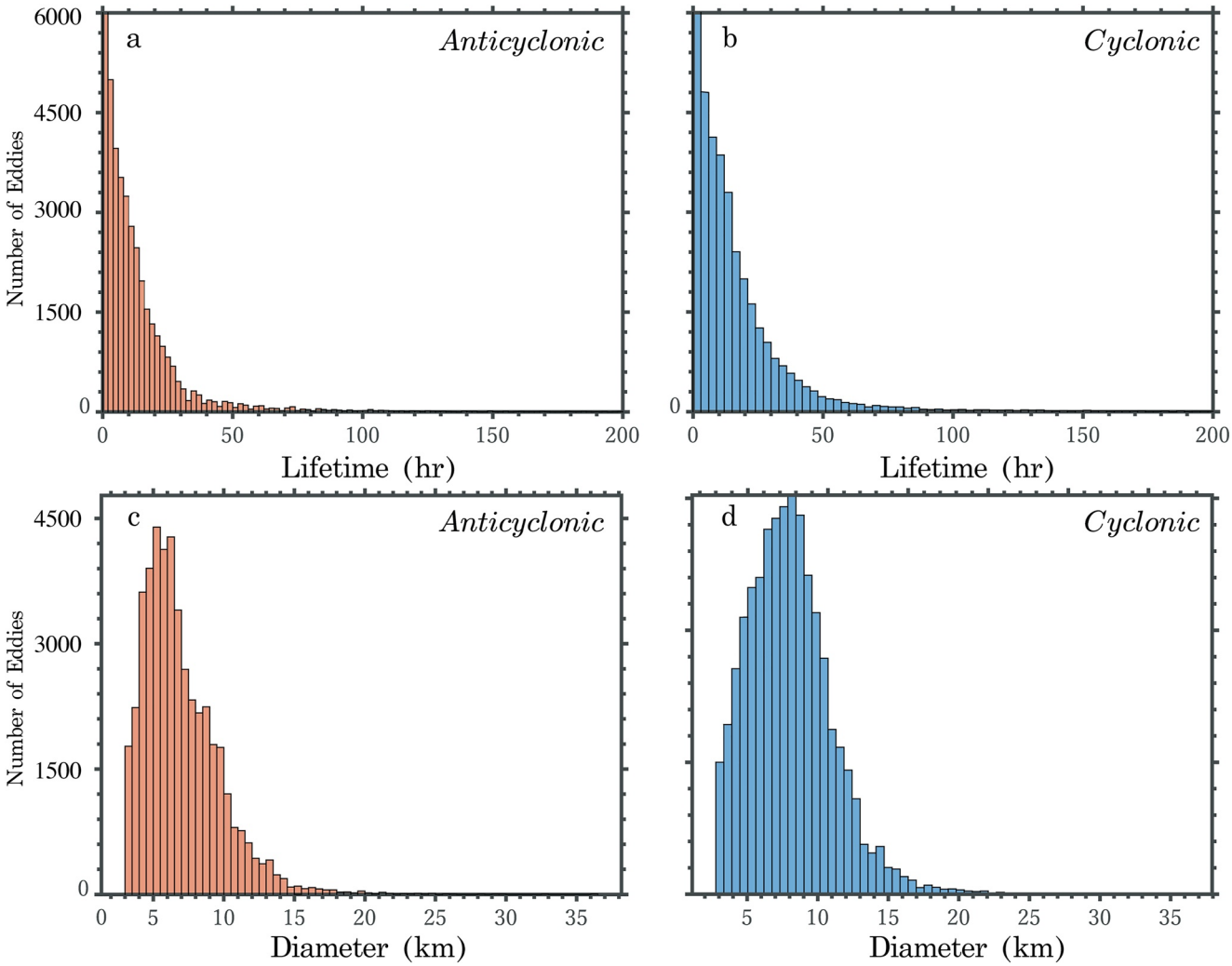

Figure 3. Histograms of the eddy lifetimes and eddy diameters for cyclonic and anticyclonic eddies.

cyclonic (51%) and anticyclonic (49%) eddies. This is because cyclonic eddies lasted longer as evidenced by the histograms of eddy lifetimes (Figure 3). Most eddies lasted less than 1 day, although some lasted up to 7 days. Few eddies had diameters greater than 20 km and cyclonic eddies were slightly larger: the modal diameter was ∼10 km for cyclonic eddies and ∼7 km for anticyclonic eddies. This size range aligns with the characterization of submesoscale eddies, considering the average deformation radius falls within the 20–30 km range (Dong & McWilliams, 2007). The histogram of normalized vorticity at the center of eddies revealed a modal value of approximately 0.6 for cyclonic eddies and −0.45 for anticyclonic eddies (Figure 4a). Monthly averaged values of normalized vorticity for both cyclonic and anticyclonic eddies exhibited similar variations, ranging from 0.5 to 0.9, and displayed similar seasonal cycles with higher values during late spring and early summer and lower values during late fall, and early winter. The observed seasonality in eddy vorticity can likely be attributed to the influence of stronger wind stress curls during spring and summer, and relatively weaker ones during winter and fall (Dong et al., 2009).

3.2. Spatial Distribution

Identifying and counting eddy occurrences are important because they (a) reveal geographical patterns such as areas of frequent eddy occurrence, (b) provide clues about the generation mechanisms, (c) provide information about the transport dynamics, and (d) suggest ecological effects such as phytoplankton transport through retention, or upwelling/downwelling within eddies. The spatial distribution of cyclonic and anticyclonic eddies

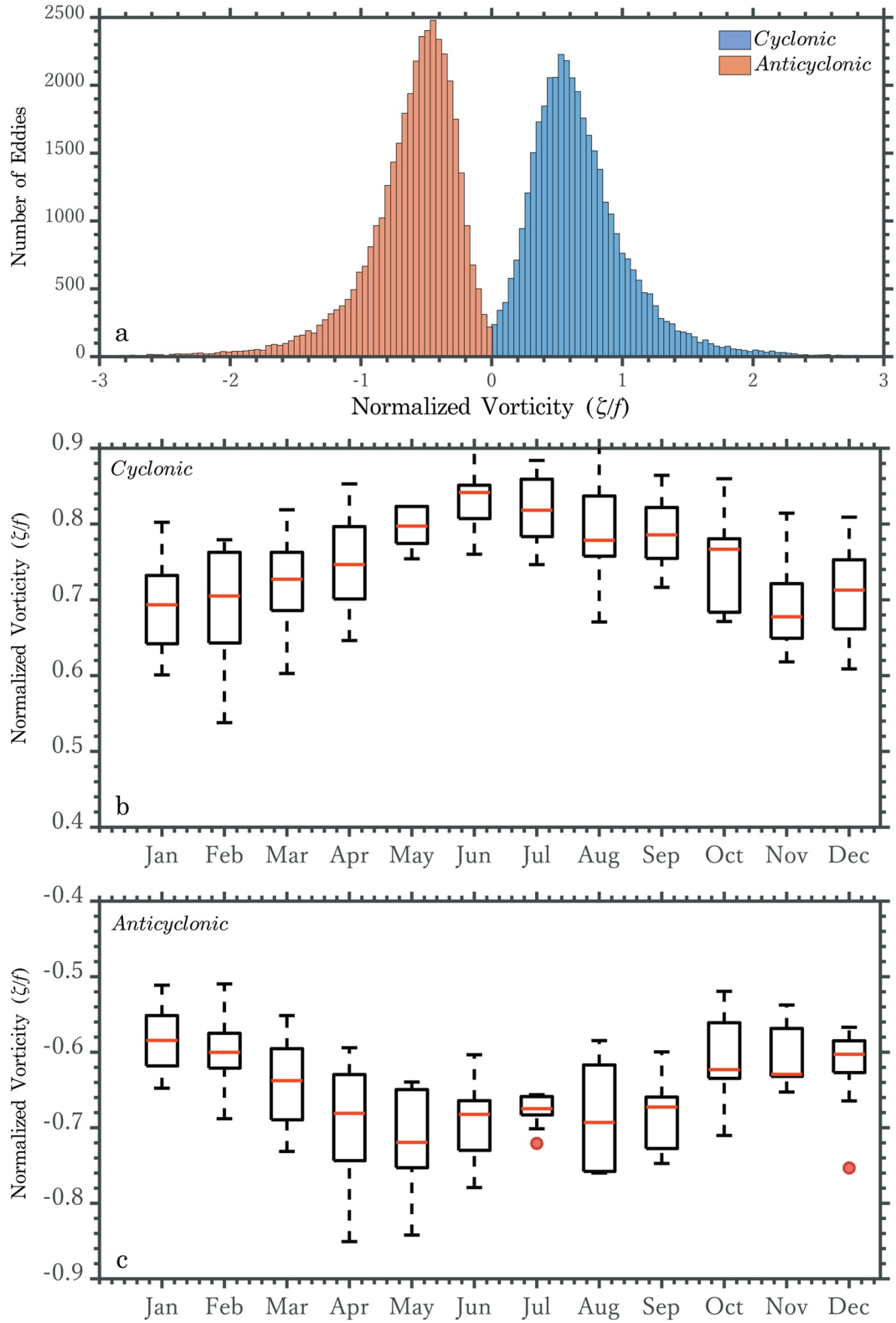

Figure 4. (a) Histogram of the normalized vorticity ζ/f at the center of eddies. Box plot of monthly averaged normalized vorticity ζ/f at the center of (b) cyclonic eddies and (c) anticyclonic eddies. Box plots show median (red bars), upper and lower quartiles (top and bottom of boxes), minimum and maximum values (vertical lines extending from boxes), and outliers (red dots).

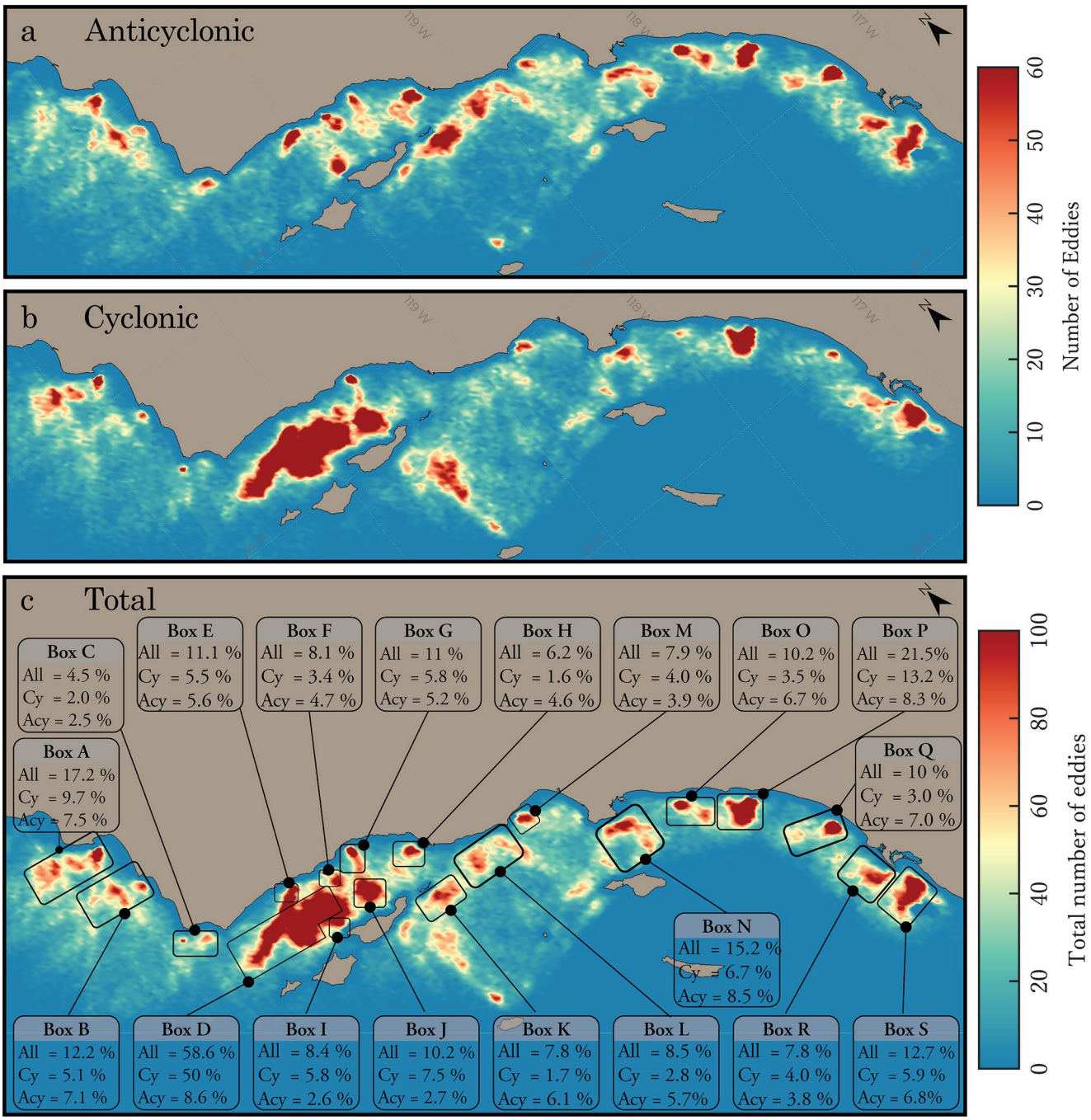

Figure 5. (a) Anticyclonic, (b) cyclonic, and (c) total eddy detections at each grid point based on hourly high-frequency radar data during 2012–2021 (87,613 hr). Hotspots of eddy activity are indicated by black boxes in panel (c). Numbers in boxes show eddy probability in each hotspot: any type (All), anticyclonic (Acy), or cyclonic (Cy). The maps are rotated 40° counterclockwise relative to true north.

revealed that eddies recurred in clusters throughout the study area (dark red areas, Figure 5). In general, clusters of anticyclonic eddies were more numerous and closer to the coastlines of the mainland and islands than cyclonic clusters. For identifying and quantifying eddy occurrence, we subjectively organized eddy clusters into 19 "hotspots" (black boxes, Figure 5c). Eddy probability λ in each hotspot b was calculated as $\lambda(b) = \delta(b)/\beta(b)$ where $\delta(b)$ is the number of hourly eddy detections in b and $\beta(b)$ is the total hours of data available in b. The most active hotspot was located in the middle of the SBCh (box D) where a channel-wide cyclonic, quasi-geostrophic eddy is a persistent feature (Beckenbach & Washburn, 2004; Harms, 1996; Harms & Winant, 1998). Eddy probability in

this hotspot was 58.6% with 50% cyclonic and 8.6% anticyclonic. These eddies either result from the large-scale cyclonic circulation in the channel or smaller propagating cyclones generated in the eastern channel that migrate westward. The channel-wide eddies are typically in geostrophic balance (Harms, 1996), extend well below the thermocline (Harms & Winant, 1998), and enhance productivity through the retention of coastal upwelled waters or eddy pumping (Brzezinski & Washburn, 2011).

The SBCh was the most consistent area for eddy formation, and it included multiple hotspots in addition to box D. This region is characterized by strong wind stress curls, headlands, islands, and complex flows, often linked to the generation of submesoscale eddies (Dong et al., 2012). Hotspots F and G in the channel appear near Campus Point (just east of the HFR site adjacent to the white dot in Figure 1) and Santa Barbara Point (just west of Santa Barbara in Figure 1). Farther west is hotspot E which does not appear to be associated with any headland. There is also a hotspot close to the western tip of Santa Cruz Island (box I) and another south of Anacapa Island (box K) which predominantly generated anticyclonic eddies. Among the Northern Channel Islands, Santa Cruz and Anacapa generated more eddies compared to Santa Rosa and San Miguel. North of Point Arguello, several hotspots were found in the lees of Point San Luis (box A), Point Sal (box B), and Point Conception (box C).

In the Santa Monica Basin, both cyclonic and anticyclonic eddies (box M) recurred near Point Dume. Also, the San Pedro Channel exhibited a high number of cyclonic and anticyclonic eddies with a 15.2% eddy probability (box N). The anticyclonic eddy generation in this region has been attributed to the poleward Southern California Countercurrent (Dauhajre et al., 2017; Marmorino et al., 2010). Another active area was near Dana Point in the southern SCB with 21.5% eddy probability, from which 13.2% was cyclonic and 8.3% was anticyclonic (box P). Between San Diego and Los Angeles, no topographic feature appeared to be related to hotspots Q and O, which are located off Oceanside and Newport Beach, respectively. Two hotspots were found off San Diego (boxes R and S), in agreement with the previous study of Kim (2010), who also found these to be preferred areas for eddy generation. Overall, the spatial distribution of eddies exhibited strong topographically related heterogeneity, in agreement with (Dong et al., 2009), who showed that eddy kinetic energy distribution is largely determined by topography in this region. Fewer eddies were found over much of the offshore area of the SCB as shown by yellow-shaded areas away from eddy hotspots.

3.3. Seasonal and Inter-Annual Variation

Monthly eddy counts indicated a seasonal cycle, with more occurrences in summer and early fall than in spring and winter (Figure 6a). The highest numbers of eddies were in August with a median of 2,320 and April had the fewest with a median of 1,490. April 2013 was the least active month with 678 eddies and August 2021 was the most active month with 2,945 eddies. The outlier in Figure 6a occurred in March 2015 during the 2015 MHW. Contrasting seasonal patterns of eddy occurrence were also discernible in spatial distributions such as in April versus August (Figures 6b and 6c, respectively). For instance, eddy hotspots north of Point Conception (boxes A, B, and C) had fewer eddies during April, the least active month, compared to August, the most active month. Eddy hotspots in the SBCh (box E), San Pedro Channel (box N), Newport Beach (box O), Dana Point (box P), Del Mar (box Q), and off the coast of San Diego (boxes R and S) showed similar seasonal differences. Previous studies conducted in the region have found that eddies occur more frequently during the summer and fall months, which is in agreement with the seasonal pattern reported in this study. The seasonal variation of eddy counts has been attributed to the seasonal variation of wind stress curl in the region (Dong et al., 2009, 2012; Kim, 2010).

The eddy-count time series exhibited inter-annual variation with a significant rise in counts between 2014 and 2016 (Figure 7a). This time period coincided with the positive phase of the Multivariate ENSO Index Version 2 (MEI.v2; T. Zhang et al., 2019; Figure 7b) and with the 2014–2015 MHW and following El Niño. A weaker El Niño occurred from mid-2018 until early 2021. Monthly and yearly averaged 5-m temperature at Naples Reef in the SBCh (white dot, Figure 1) showed that 2014 and 2015 were the warmest years during the study period (Figure 7c). The average 5-m temperature rose by 1.6°C between 2013 and 2014, while the eddy counts rose by 40%, mostly due to increased anticyclonic eddies (Figure 7a). In 2015, the average 5-m temperature rose by an additional 0.5°C compared to 2014, while anticyclonic eddy counts increased slightly. These changes made 2015 the warmest year of the study period and the most active year for anticyclonic eddies. In 2016, the negative phase of the MEI.v2 began, corresponding to a decrease in total eddy counts that year and a 25% drop in eddy counts the following year (2017).

Accompanying increased eddy activity during 2014–2016 were higher sea surface temperature (SST) anomalies which rose to ~2°C in 2015 throughout the SCB (Appendix A, Figure A1). At the same time, increases in

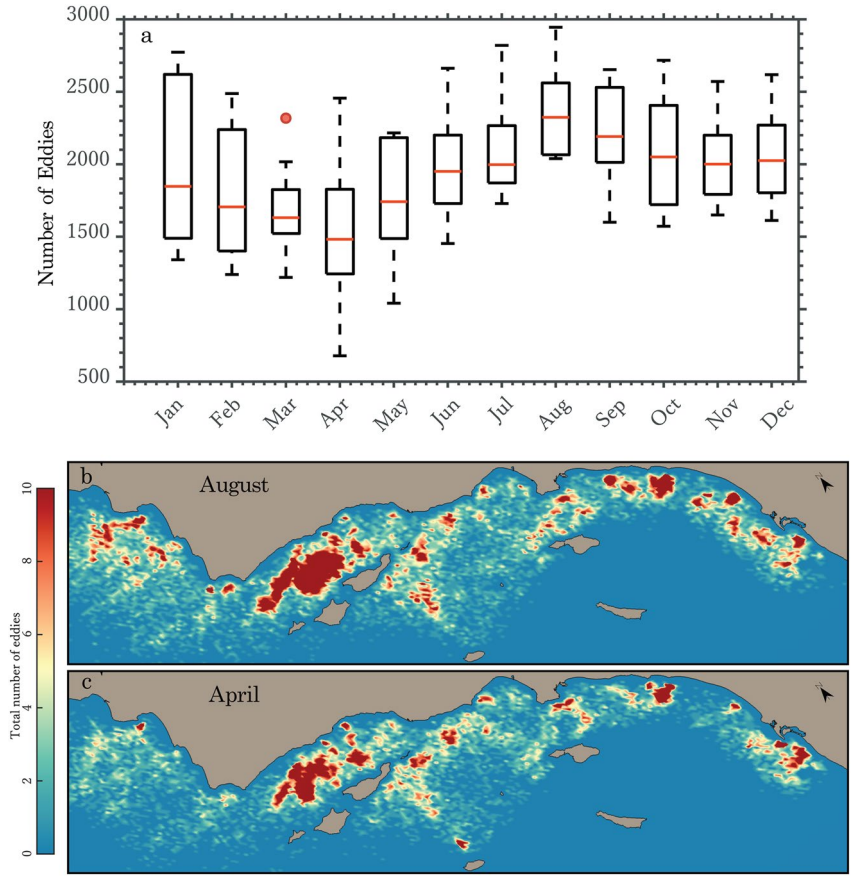

Figure 6. Box plot of (a) monthly sum of hourly eddy detections. Monthly spatial distribution of eddies for (b) August and (c) April. The maps are rotated 40° counterclockwise relative to true north.

eddy-occurrence anomalies concentrated in eddy hotspots with greater numbers and a broader distribution of anticyclonic eddies compared to cyclonic eddies (Figure 8). An increase in the number of eddies was not reproduced during the weak El Niño event of 2018–2020, nor was an increase in temperature, suggesting that this event did not significantly impact atmospheric and oceanographic conditions in the SCB (Figure 7).

The inter-annual variability in eddy counts may be attributed to shifts in wind and circulation patterns resulting from the 2014–2015 MHW. Bond et al. (2015) found that the wind stress curl was unusually negative in the SCB during the 2014–2015 MHW, providing a possible explanation for the higher anticyclonic eddies during this period. Weak positive wind stress curl is also typical during the fall when anticyclonic eddies become more common (Winant & Dorman, 1997). In the absence of strong northwesterly winds, the fall season typically experiences a strong poleward current. This poleward current can induce negative vorticity through interactions with topography, leading to the formation of anticyclonic eddies, as discussed by Gula et al. (2016) in the context of the Gulf Stream. Our findings indicate that in 2014 and 2015, the poleward flow reached its peak strength (Figure 9). This observation suggests that the intensified poleward flow could have contributed to the heightened occurrence of anticyclonic eddies during the 2014–2015 MHW.

The inter-annual pattern we observed is consistent with (Dong et al., 2009), who examined mesoscale activity in the SCB using ROMS for the years 1996–2003. They found that eddy kinetic energy during these years was highest in 1997–1998 and associated with a strong ENSO event. Escalating influence of MHWs and El Niño on eddy activity is likewise observed in other parts of the world. The Tasman Sea exhibited its most prolonged (251 days) and severe MHW ever recorded in 2015–2016. Eddy kinetic energy in this region was elevated in 2015–2016 compared to the preceding 3 years (Oliver et al., 2017). Modeling studies of ocean conditions from 1958 to 2008 along the coast of Peru have shown a rise in eddy activity during El Niño events, especially during the extreme events of 1972–1973, 1982–1983, and 1997–1998 (Espinoza-Morriberón et al., 2017). In their study

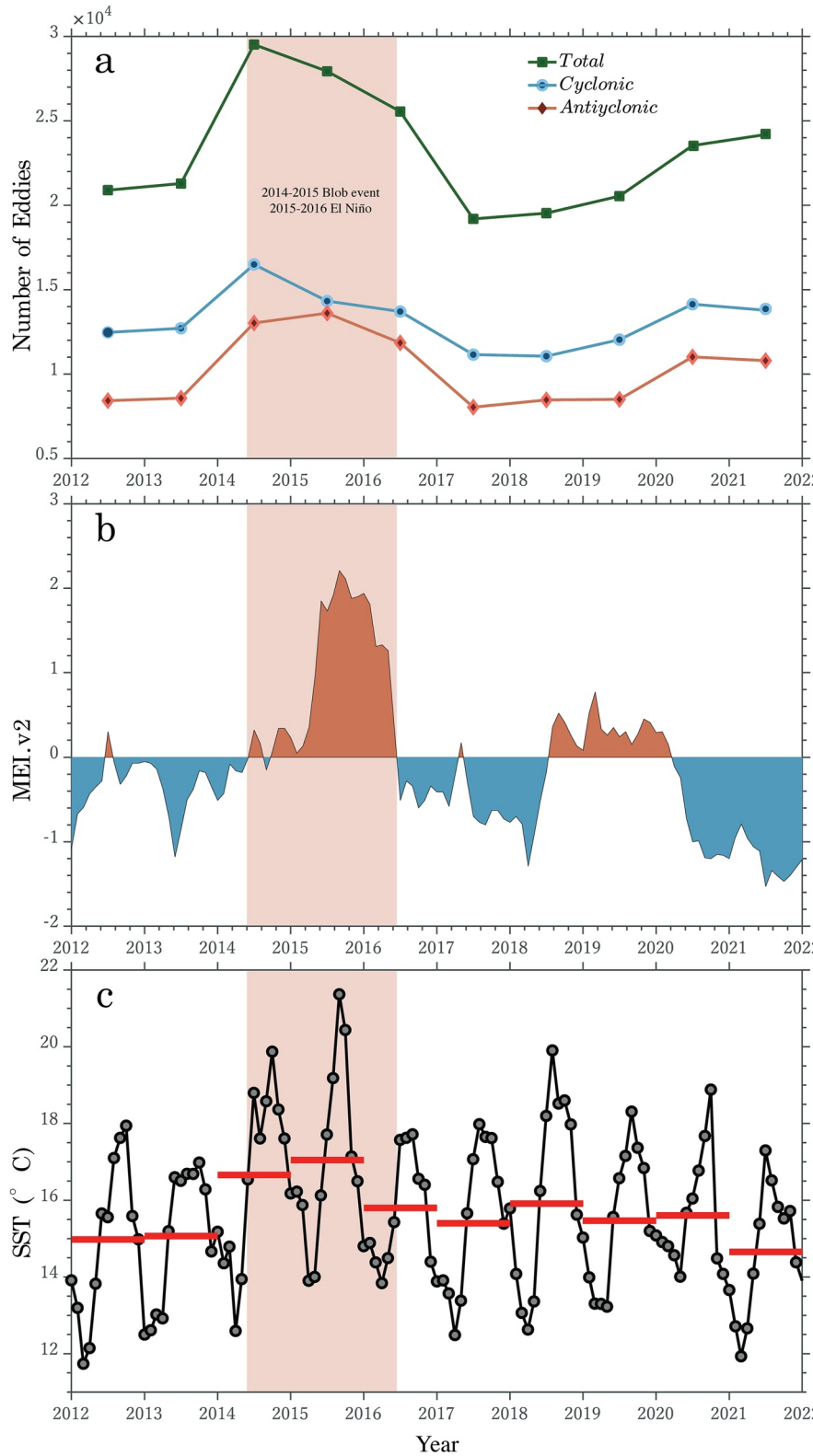

Figure 7. (a) Annual counts of the total, cyclonic, and anticyclonic eddies, (b) time series of Multivariate ENSO Index Version 2, (c) times series of monthly averaged 5-m temperature at Naples Reef (white circle, Figure 1). Red lines indicate the yearly average of 5-m temperature. Temperature data were obtained from a moored CTD at Naples Reef at ~5-m depth (10 m above bottom). Tan shaded areas indicate times of the 2014–2015 MHW and the 2015–2016 El Niño.

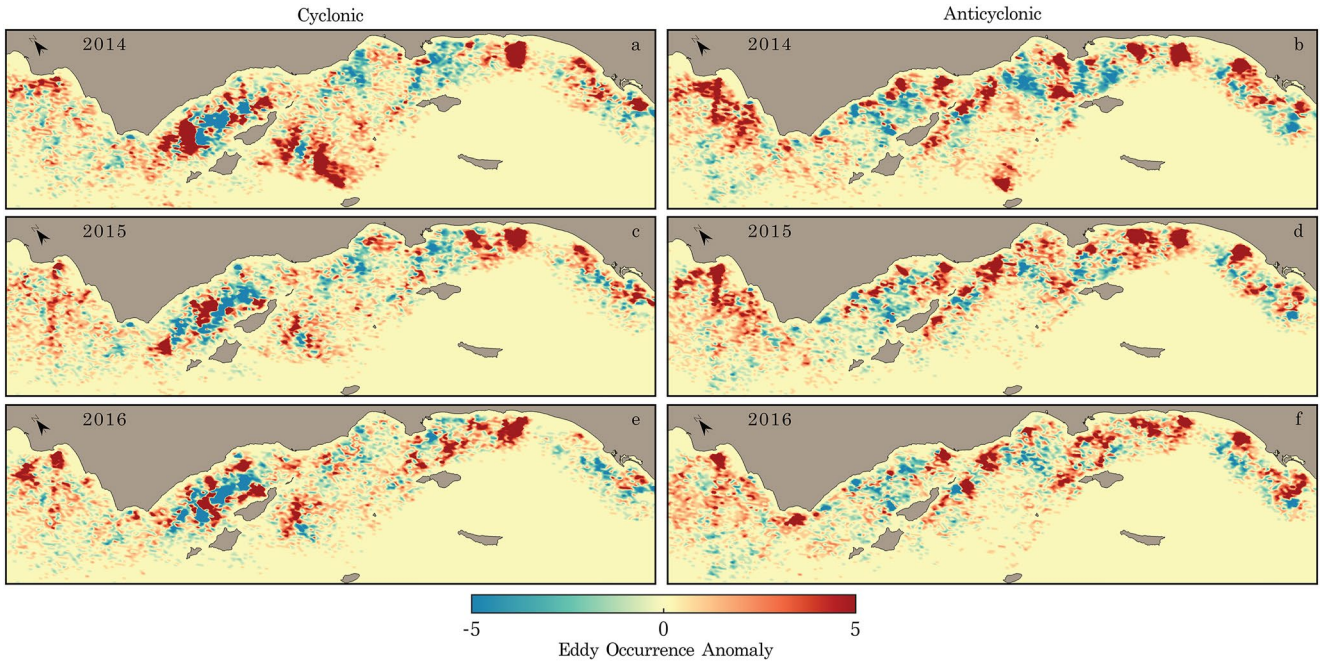

Figure 8. Eddy occurrence anomalies of cyclonic (panels a, c, and e) and anticyclonic eddies (panels b, d, and e). Anomalies were calculated relative to the mean annual eddy occurrences from 2012 to 2021. Color bar shows scale for anomalies. Yellow areas indicate zero occurrence anomalies or areas with no data. The maps are rotated 40° counterclockwise relative to true north.

of mesoscale variability in the Peru-Chile Current from 1992 to 2006, Chaigneau et al. (2008) found that the eddy counts were maximal during the El Niño of 1997–1998. Conejero et al. (2020) found that eddy activity along the Peruvian coast tends to increase during strong Eastern Pacific El Niño events, but is hardly changed during Central Pacific El Niño events.

3.4. Diurnal and Semi-Diurnal Variability

A clear diurnal cycle was observed in the time series of normalized vorticity across the study area. Figure 10a provides an example in hotspot P where the normalized vorticity exhibits a diurnal cycle, with a distinct pattern of one high and one low value every 24 hr. Cyclonic and anticyclonic eddies were identified in conjunction with the peaks and troughs in vorticity. These eddies lasted only a few hours before dissipating. Variations in vorticity and eddy formation corresponded to daily fluctuations in wind stress. The power spectrum of normalized vorticity at the same point as the time series of Figure 10a revealed a large diurnal peak and smaller semidiurnal peak. Spectra of wind stress and occurrences of cyclonic and anticyclonic eddies within hotspot P, also displayed large diurnal and smaller semidiurnal peaks (Figures 10c and 10e).

Conditional averaging of recurrent eddies in hotspot P allows visualization of the structure and diurnal evolution of these eddies. In the conditional averaging approach, surface currents were ensemble-averaged over many eddy occurrences for each time 0 when eddy centers were detected in this hotspot. This averaging was then repeated for times before and after time 0 to see eddy development. The approach was applied separately to cyclonic and anticyclonic eddies occurring in hotspot P (Figure 11). Over the 10 years of HFR data, a total of 4,978 cyclonic and 2,983 anticyclonic eddies were identified within hotspot P. Consequently, 4,978 and 2,983 hourly HFR frames were averaged at each hour for cyclonic and anticyclonic eddies, respectively. The conditional averaging of currents revealed a consistent pattern of eddy formation every 24 hr before and after time 0. Furthermore, normalized vorticity values indicated that the minimum occurred approximately 12 hr before eddy generation, while the highest values were observed at the 24-hr mark. Hotspot P is representative of other hotspots exhibiting recurring eddies. Similarly, conditionally averaged currents in other hotspots demonstrated analogous diurnal patterns in cyclonic and anticyclonic eddy formation, as well as normalized vorticity variation, throughout the study area.

Resolving spectral components at diurnal and semidiurnal frequencies provides insights into the possible forcing mechanisms (e.g., tides vs. wind) that drive vorticity variation. Along the SCB (red line, Figure 12a), the power

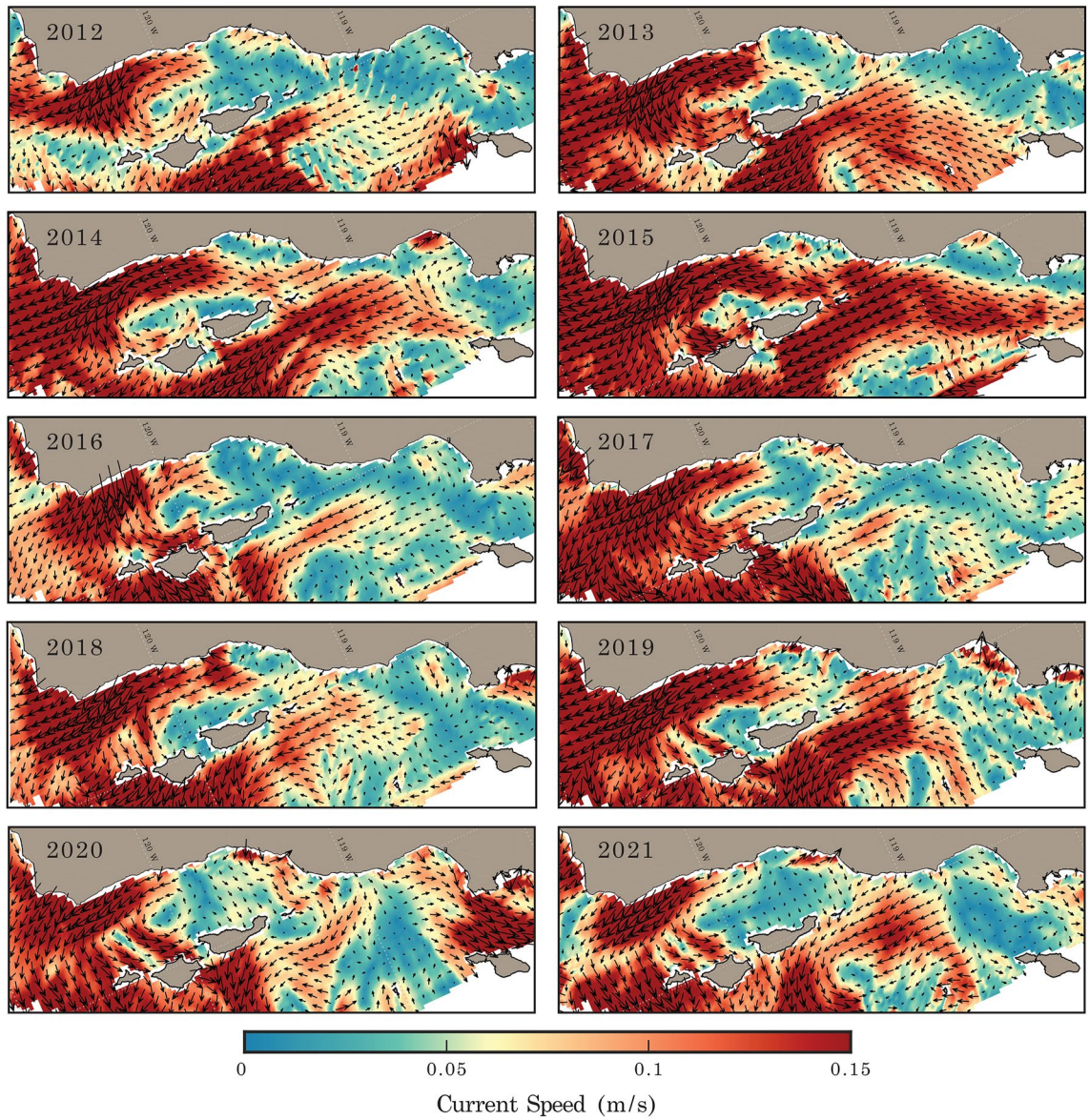

Figure 9. Average fall season current speed in the central Southern California Bight from 2012 to 2021.

spectrum of normalized vorticity displayed prominent diurnal peaks at K_1, O_1, and S_1 as well as semidiurnal peaks at M_2, S_2, and N_2 (Figure 12b). Even though the availability of data along the SCB coastline varies and this affects the power spectrum estimation (Figure 12c), variance at individual frequencies can still be compared at each point. These comparisons showed that the S_1 frequency dominates in most locations along the SCB, except for a few areas where the M_2 frequency dominates (Figure 13b). The ocean experiences a negligible astronomical tide at exactly one cycle per solar day, the S_1 frequency. The S_1 tide is an example of a "meteorological" tide and the primary cause of fluctuations at this frequency is believed to be related to the diurnal sea-land breeze (e.g., Munk & Cartwright, 1966; Ray & Egbert, 2004; Schureman, 1958). Therefore, the prevalence of the S_1 frequency along the SCB suggests that the diurnal cycle in normalized vorticity and eddy generation is primarily driven by sea-land breeze.

Diurnal variance in normalized vorticity ($K_1 + O_1 + S_1$) was larger than semidiurnal variance ($M_2 + S_2 + N_2$) over most of the SCB (Figure 13). The few areas where M_2 variance was larger included north of Point Conception, south of Point Sal, north of Point Dume, and a few points off the coast of San Diego. Near hotspot P offshore of Dana Point, there was a large spike in diurnal variance that greatly exceeded semidiurnal variance. The highest power spectral amplitudes at frequency S_1 were also observed south of Dana Point. Among tidal constituents K_1,

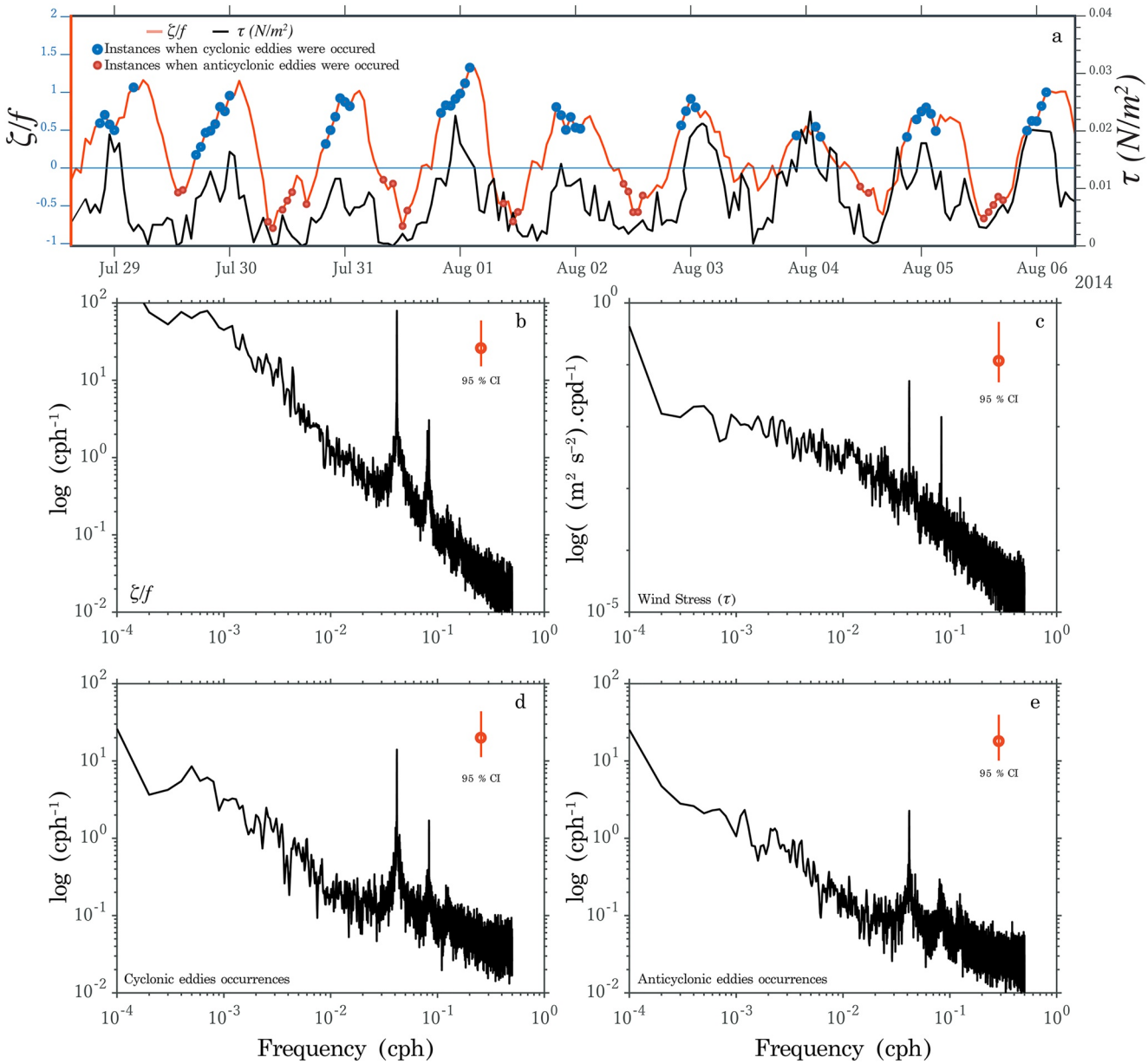

Figure 10. (a) Example of ζ/f time series at a point at the center of hotspot P (left axis) and wind stress (τ) time series (right axis). Blue and red circles show instances when cyclonic and anticyclonic eddies occurred, respectively. Wind data were obtained from the National Data Buoy Center at Station LJPC1. Power spectra of (b) ζ/f, (c) wind stress (τ), (d) cyclonic eddy occurrences, and (e) anticyclonic eddy occurrences, obtained from the whole 10 years of the study period. The 95% confidence interval (CI) of each spectrum is indicated.

O_1, M_2, S_2, and N_2, the highest variances were at frequencies M_2 and K_1. Starting from the south, K_1 was found to be larger south of San Diego, while M_2 was larger off San Diego (Figure 13b). Toward the north, K_1 was larger north of San Diego and south of Point Dume. Between Point Dume and the eastern Santa Barbara Channel, M_2 was the largest tidal frequency, while in the central and western Santa Barbara Channel, K_1 was the largest. North of Point Conception, the largest tidal frequency was M_2.

4. Summary and Conclusion

HFR-derived surface current measurements provide an observational resource to examine the surface expression of submesoscale eddies. A decade of these observations (2012–2021) revealed the widespread existence of submesoscale eddies in the SCB. By creating spatial distribution maps encompassing ~235,000 hourly

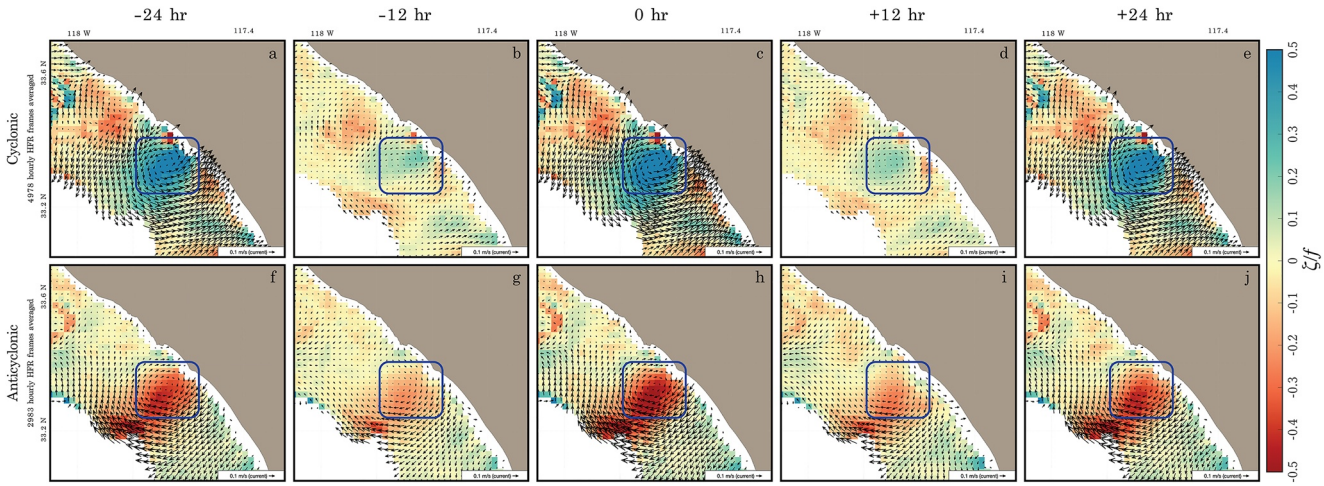

Figure 11. Conditionally averaged currents based on (a–e) cyclonic eddies and (f–j) anticyclonic eddies occurring in hotspot P (blue box). Rows show averaged currents from 24 hr before to 24 hr after day 0 when eddies were detected in hotspots indicated by blue boxes.

eddy detections, we demonstrated how topography largely shapes the spatial variability of these eddies. The record revealed that eddies were more numerous in summer and early fall compared with spring and winter. At inter-annual scales, the data set showed that the eddy numbers increased by 40% during the 2014–2015 MHW and the 2015–2016 El Niño. These findings raise important issues that require further investigation, such as exploring the mechanisms that contribute to the seasonal variability of submesoscale eddies. Additionally, understanding the impact of the MHWs and El Niño events on atmospheric and oceanographic conditions in the SCB is crucial in understanding why eddy activity increased during the prolonged period of 2014–2016. A specific question that arises from these findings is why anticyclonic eddies increased more than cyclonic eddies during this event. Our results indicated the poleward flow exhibited its peak strength during 2014 and 2015. This poleward flow has the capacity to generate negative vorticity through its interaction with topography, leading to the formation of more anticyclonic eddies. However, HFR data that are the basis for this study do not provide sufficient information from which to fully diagnose the underlying mechanisms of eddy generation and their evolving dynamic balances. Therefore, gaining a deeper understanding of the mechanisms driving the inter-annual variations of submesoscale eddies will require further investigation through numerical modeling.

The conditional averaging technique revealed that both the normalized vorticity and the formation of submesoscale eddies exhibited a diurnal cycle across the entire domain. This observation was further supported by power spectral analysis of the normalized vorticity, which demonstrated peaks at both diurnal and semidiurnal frequencies with the diurnal frequency being dominant. Diurnal motions have also been previously observed in the SCB (Beckenbach & Terrill, 2008; Cudaback & McPhee-Shaw, 2009; Kumar et al., 2016; Lerczak et al., 2001; Nam & Send, 2013) and diagnosed in ROMS (Dauhajre et al., 2017; Dauhajre & McWilliams, 2018; Kumar et al., 2016). They have been attributed to the surface heating/cooling cycle (Dauhajre & McWilliams, 2018), sea-land breeze (Kumar et al., 2016; Nam & Send, 2013), barotropic tides (Beckenbach & Terrill, 2008) and subtidal vorticity reducing the effective Coriolis frequency below diurnal (Lerczak et al., 2001).

By comparing the spectral components and their spatial variations along the SCB, we were able to assess the relative importance of tides and diurnal wind. Our findings indicated that while diurnal tides may have some influence on the diurnal variations observed in eddy formations, their impact is minor compared to diurnal winds. This conclusion was drawn based on the prevalence of the S_1 frequency in most locations along the SCB, which is known to be associated with motions induced by diurnal winds. In addition to S_1, tidal frequencies of M_2 and K_1 were significant in the vorticity spectra, with their relative spectral amplitudes changing along the SCB.

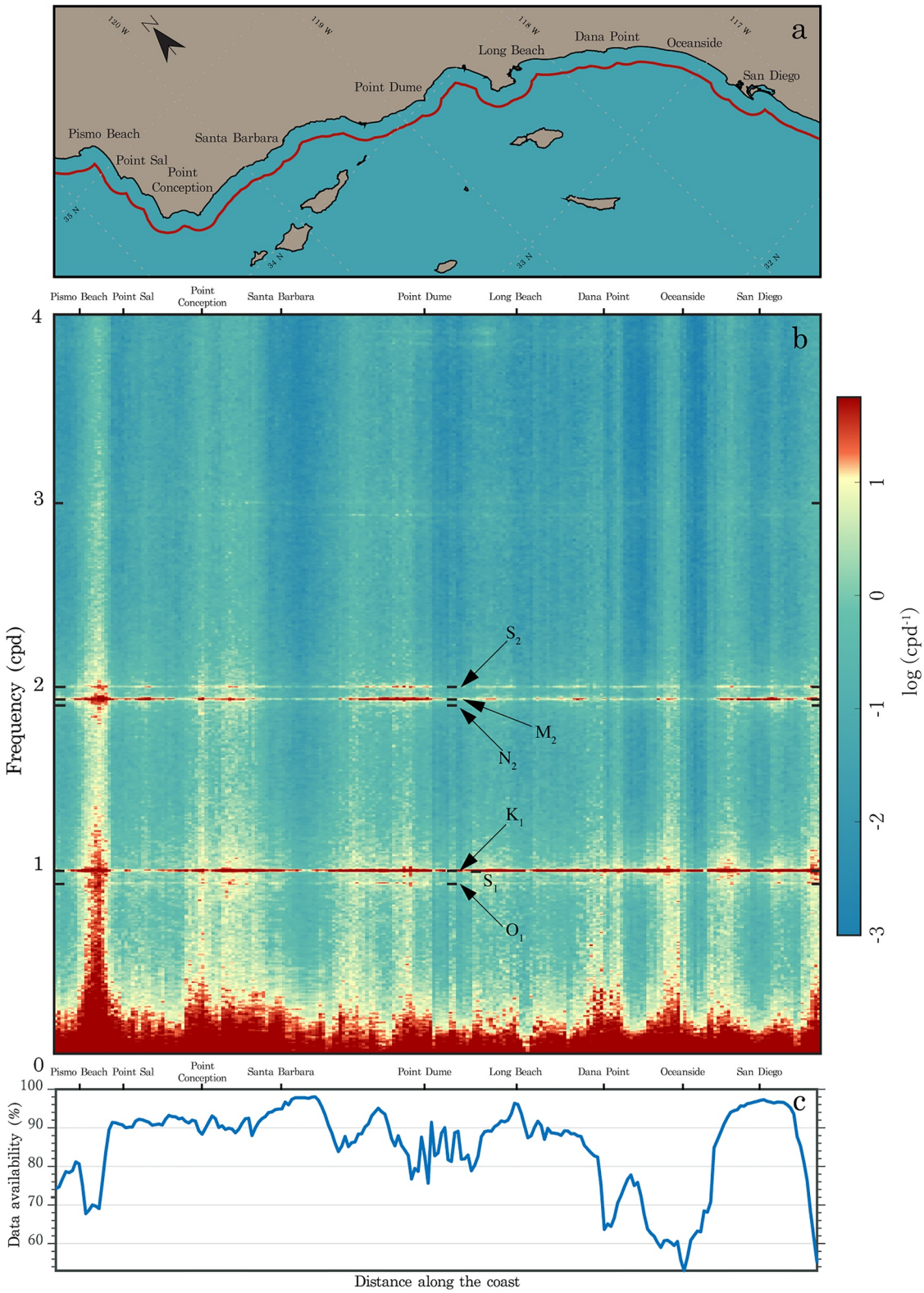

Figure 12. (a) Map of the Southern California Bight with a red line positioned 10 km from the shore where the power spectra are calculated along its length. (b) Power spectra of ζ/f along the red line shown in panel (a). (c) Data availability at each grid point along the red line.

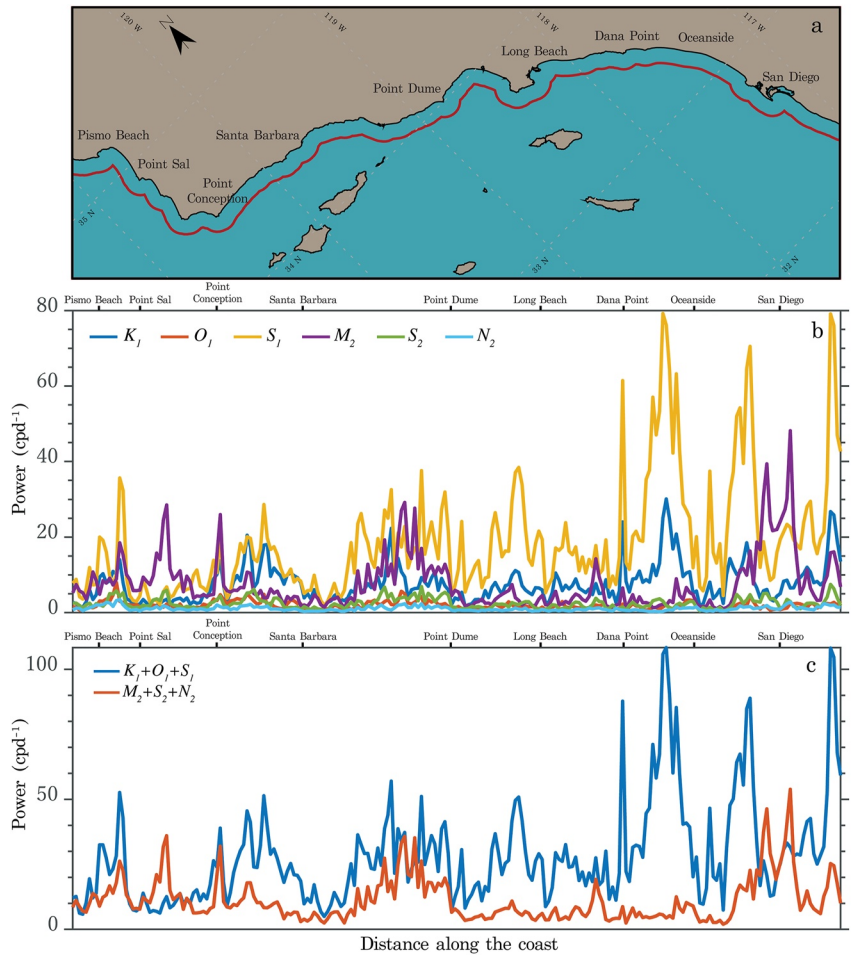

Figure 13. (a) Map of the Southern California Bight with a red line positioned 10 km from the shore where the power spectra are calculated. (b) Power spectral variance of ζ/f along the red line at diurnal and semidiurnal frequencies. (c) The sum of the power spectral variance of ζ/f at diurnal and semidiurnal frequencies.

In our ongoing research, we aim to further explore the potential contribution of other mechanisms, previously mentioned, to the diurnal cycle observed in the generation of submesoscale eddies within the SCB. Our focus will extend to examining the spatial variability of this diurnal cycle and the underlying factors, with a specific emphasis on the southern SCB, where the diurnal variability is particularly pronounced. Moreover, we will investigate the connections between kelp forest ecosystems and the cross-shore water-volume transport facilitated by submesoscale eddies along the highly productive coasts of the SCB. These future research directions will leverage the capabilities of HFRs to continuously observe surface currents over large spatial domains and extended time periods.

Appendix A: MHW Anomaly

Figure A1 presents the seasonal SST anomalies observed in the SCB from 2014 to 2017. SST data were derived from a daily, global 1-km SST data set (GHRSST, Level 4), and anomalies were calculated relative to the mean seasonal sea surface temperature during the study period (2012–2021). The MHW commenced during the winter of 2014 and gradually intensified, reaching its peak in 2015. The influence of El Niño led to sustained higher SST values in 2016, followed by dissipation within the same year.

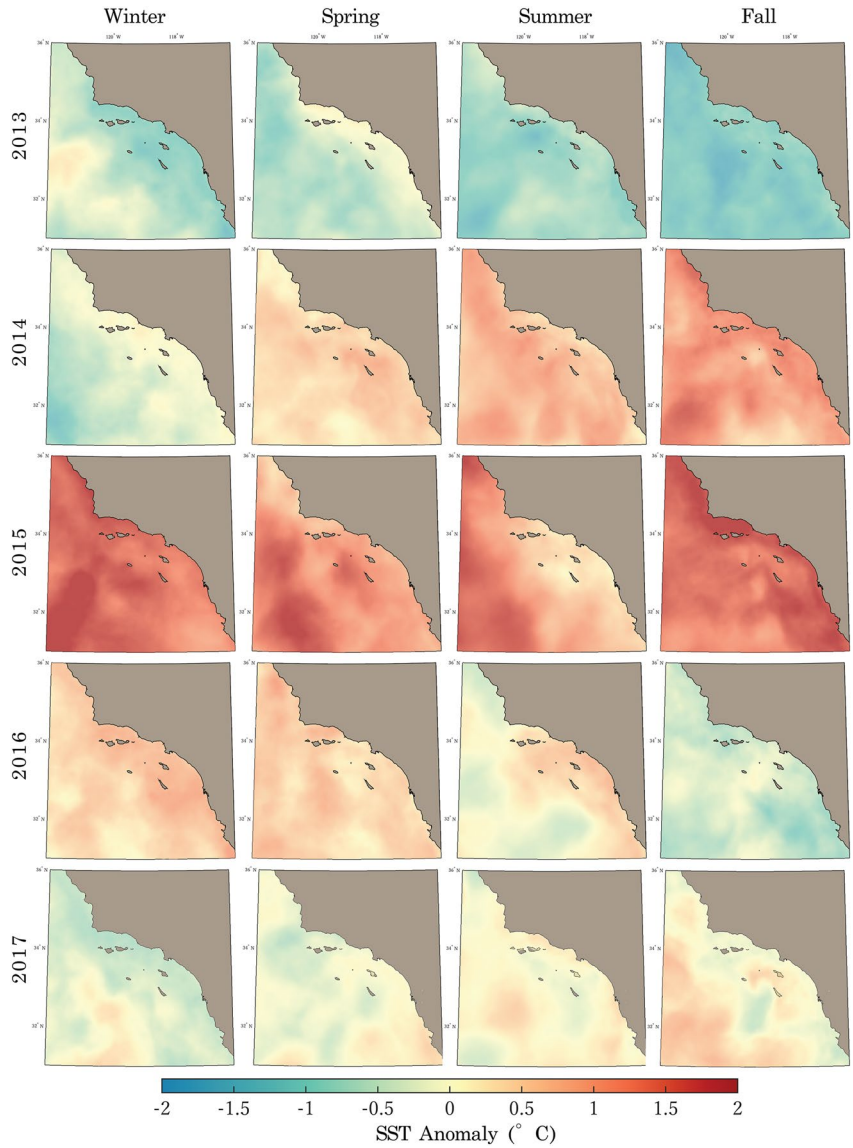

Figure A1. Seasonal sea surface temperature anomalies from 2014 to 2017.

Data Availability Statement

Data used in this study are made available by the Coastal Observing Research and Development Center at the Scripps Institution of Oceanography (CORDC). CORDC runs a Thematic Real-Time Environmental Distributed Data Services (THREDDS) Data Server, using standard remote data access protocols https://hfrnet-tds.ucsd.edu/thredds/catalog.html.

Acknowledgments
This work was supported in part by the National Science Foundation under Grant OCE-1658475 and OCE-1923465. The funding was also provided by the NOAA Integrated Ocean Observing System through the Southern California Coastal Ocean Observing System (SCCOOS; https://sccoos.org/). The authors thank the many technicians and students who help maintain the radars, moorings, and other infrastructure of SCCOOS and SBC LTER.

References

Bassin, C. J., Washburn, L., Brzezinski, M., & McPhee-Shaw, E. (2005). Sub-mesoscale coastal eddies observed by high frequency radar: A new mechanism for delivering nutrients to kelp forests in the Southern California Bight. *Geophysical Research Letters*, *32*(12), L12604. https://doi.org/10.1029/2005gl023017

Beckenbach, E., & Terrill, E. (2008). Internal tides over abrupt topography in the Southern California Bight: Observations of diurnal waves poleward of the critical latitude. *Journal of Geophysical Research: Oceans*, *113*(C2), C02001. https://doi.org/10.1029/2006jc003905

Beckenbach, E., & Washburn, L. (2004). Low-frequency waves in the Santa Barbara Channel observed by high-frequency radar. *Journal of Geophysical Research: Oceans*, *109*(C2), C02010. https://doi.org/10.1029/2003jc001999

Bond, N. A., Cronin, M. F., Freeland, H., & Mantua, N. (2015). Causes and impacts of the 2014 warm anomaly in the NE Pacific. *Geophysical Research Letters*, *42*(9), 3414–3420. https://doi.org/10.1002/2015gl063306

Brzezinski, M. A., & Washburn, L. (2011). Phytoplankton primary productivity in the Santa Barbara Channel: Effects of wind-driven upwelling and mesoscale eddies. *Journal of Geophysical Research: Oceans*, *116*(C12), C12013. https://doi.org/10.1029/2011jc007397

Caldeira, R. M., Marchesiello, P., Nezlin, N. P., DiGiacomo, P. M., & McWilliams, J. C. (2005). Island wakes in the Southern California Bight. *Journal of Geophysical Research: Oceans*, *110*(C11), C11012. https://doi.org/10.1029/2004jc002675

Capet, X., Campos, E., & Paiva, A. (2008). Submesoscale activity over the Argentinian shelf. *Geophysical Research Letters*, *35*(15), L15605. https://doi.org/10.1029/2008gl034736

Chaigneau, A., Gizolme, A., & Grados, C. (2008). Mesoscale eddies off Peru in altimeter records: Identification algorithms and eddy spatio-temporal patterns. *Progress in Oceanography*, *79*(2–4), 106–119. https://doi.org/10.1016/j.pocean.2008.10.013

Chenillat, F., Franks, P. J., Rivière, P., Capet, X., Grima, N., & Blanke, B. (2015). Plankton dynamics in a cyclonic eddy in the Southern California Current System. *Journal of Geophysical Research: Oceans*, *120*(8), 5566–5588. https://doi.org/10.1002/2015jc010826

Conejero, C., Dewitte, B., Garçon, V., Sudre, J., & Montes, I. (2020). ENSO diversity driving low-frequency change in mesoscale activity off Peru and Chile. *Scientific Reports*, *10*(1), 1–13. https://doi.org/10.1038/s41598-020-74762-x

Cudaback, C. N., & McPhee-Shaw, E. (2009). Diurnal-period internal waves near point conception, California. *Estuarine, Coastal and Shelf Science*, *83*(3), 349–359. https://doi.org/10.1016/j.ecss.2008.12.018

Dauhajre, D. P., & McWilliams, J. C. (2018). Diurnal evolution of submesoscale front and filament circulations. *Journal of Physical Oceanography*, *48*(10), 2343–2361. https://doi.org/10.1175/jpo-d-18-0143.1

Dauhajre, D. P., McWilliams, J. C., & Uchiyama, Y. (2017). Submesoscale coherent structures on the continental shelf. *Journal of Physical Oceanography*, *47*(12), 2949–2976. https://doi.org/10.1175/jpo-d-16-0270.1

DiGiacomo, P. M., & Holt, B. (2001). Satellite observations of small coastal ocean eddies in the Southern California Bight. *Journal of Geophysical Research: Oceans*, *106*(C10), 22521–22543. https://doi.org/10.1029/2000jc000728

Dong, C., Idica, E. Y., & McWilliams, J. C. (2009). Circulation and multiple-scale variability in the Southern California Bight. *Progress in Oceanography*, *82*(3), 168–190. https://doi.org/10.1016/j.pocean.2009.07.005

Dong, C., Lin, X., Liu, Y., Nencioli, F., Chao, Y., Guan, Y., et al. (2012). Three-dimensional oceanic eddy analysis in the Southern California Bight from a numerical product. *Journal of Geophysical Research: Oceans*, *117*(C7), C00H14. https://doi.org/10.1029/2011jc007354

Dong, C., & McWilliams, J. C. (2007). A numerical study of island wakes in the Southern California Bight. *Continental Shelf Research*, *27*(9), 1233–1248. https://doi.org/10.1016/j.csr.2007.01.016

Emery, B., & Washburn, L. (2019). Uncertainty estimates for SeaSonde HF radar ocean current observations. *Journal of Atmospheric and Oceanic Technology*, *36*(2), 231–247. https://doi.org/10.1175/jtech-d-18-0104.1

Emery, B., Washburn, L., & Harlan, J. A. (2004). Evaluating radial current measurements from CODAR high-frequency radars with moored current meters. *Journal of Atmospheric and Oceanic Technology*, *21*(8), 1259–1271. https://doi.org/10.1175/1520-0426(2004)021<1259:ercmfc>2.0.co;2

Espinoza-Morriberón, D., Echevin, V., Colas, F., Tam, J., Ledesma, J., Vásquez, L., & Graco, M. (2017). Impacts of El Niño events on the Peruvian upwelling system productivity. *Journal of Geophysical Research: Oceans*, *122*(7), 5423–5444. https://doi.org/10.1002/2016jc012439

Graber, H. C., Haus, B. K., Chapman, R. D., & Shay, L. K. (1997). HF radar comparisons with moored estimates of current speed and direction: Expected differences and implications. *Journal of Geophysical Research: Oceans*, *102*(C8), 18749–18766. https://doi.org/10.1029/97jc01190

Gula, J., Molemaker, M., & McWilliams, J. (2015). Topographic vorticity generation, submesoscale instability and vortex street formation in the Gulf Stream. *Geophysical Research Letters*, *42*(10), 4054–4062. https://doi.org/10.1002/2015gl063731

Gula, J., Molemaker, M. J., & McWilliams, J. C. (2016). Topographic generation of submesoscale centrifugal instability and energy dissipation. *Nature Communications*, *7*(1), 12811. https://doi.org/10.1038/ncomms12811

Harms, S. (1996). *Circulation induced by winds and pressure gradients in the Santa Barbara Channel*. University of California.

Harms, S., & Winant, C. D. (1998). Characteristic patterns of the circulation in the Santa Barbara Channel. *Journal of Geophysical Research: Oceans*, *103*(C2), 3041–3065. https://doi.org/10.1029/97jc02393

Hickey, B. M. (1993). Chapter 2. Physical oceanography. In M. D. Dailey, D. J. Reish, & J. W. Anderson (Eds.), *Ecology of the Southern California Bight* (pp. 19–70). University of California Press. https://doi.org/10.1525/9780520322400-006

Kim, S. Y. (2010). Observations of submesoscale eddies using high-frequency radar-derived kinematic and dynamic quantities. *Continental Shelf Research*, *30*(15), 1639–1655. https://doi.org/10.1016/j.csr.2010.06.011

Kim, S. Y., Terrill, E. J., Cornuelle, B. D., Jones, B., Washburn, L., Moline, M. A., et al. (2011). Mapping the US West coast surface circulation: A multiyear analysis of high-frequency radar observations. *Journal of Geophysical Research: Oceans*, *116*(C3), C03011. https://doi.org/10.1029/2010jc006669

Kirincich, A. (2016). The occurrence, drivers, and implications of submesoscale eddies on the Martha's Vineyard inner shelf. *Journal of Physical Oceanography*, *46*(9), 2645–2662. https://doi.org/10.1175/jpo-d-15-0191.1

Kirincich, A., & Lentz, S. (2017). The importance of lateral variability on exchange across the inner shelf south of Martha's Vineyard, MA. *Journal of Geophysical Research: Oceans*, *122*(3), 2360–2381. https://doi.org/10.1002/2016jc012491

Kumar, N., Feddersen, F., Suanda, S., Uchiyama, Y., & McWilliams, J. (2016). Mid-to inner-shelf coupled ROMS–SWAN model–data comparison of currents and temperature: Diurnal and semidiurnal variability. *Journal of Physical Oceanography*, *46*(3), 841–862. https://doi.org/10.1175/jpo-d-15-0103.1

Lai, Y., Zhou, H., Yang, J., Zeng, Y., & Wen, B. (2017). Submesoscale eddies in the Taiwan Strait observed by high-frequency radars: Detection algorithms and eddy properties. *Journal of Atmospheric and Oceanic Technology*, *34*(4), 939–953. https://doi.org/10.1175/jtech-d-16-0160.1

Lerczak, J. A., Hendershott, M., & Winant, C. (2001). Observations and modeling of coastal internal waves driven by a diurnal sea breeze. *Journal of Geophysical Research: Oceans*, *106*(C9), 19715–19729. https://doi.org/10.1029/2001jc000811

Lévy, M., Ferrari, R., Franks, P. J., Martin, A. P., & Rivière, P. (2012). Bringing physics to life at the submesoscale. *Geophysical Research Letters*, *39*(14), L14602. https://doi.org/10.1029/2012gl052756

Mahadevan, A. (2006). Modeling vertical motion at ocean fronts: Are nonhydrostatic effects relevant at submesoscales? *Ocean Modelling*, *14*(3–4), 222–240. https://doi.org/10.1016/j.ocemod.2006.05.005

Mahadevan, A. (2016). The impact of submesoscale physics on primary productivity of plankton. *Annual Review of Marine Science*, *8*(1), 161–184. https://doi.org/10.1146/annurev-marine-010814-015912

Mahadevan, A., & Tandon, A. (2006). An analysis of mechanisms for submesoscale vertical motion at ocean fronts. *Ocean Modelling*, *14*(3–4), 241–256. https://doi.org/10.1016/j.ocemod.2006.05.006

Marmorino, G. O., Holt, B., Molemaker, M. J., DiGiacomo, P. M., & Sletten, M. A. (2010). Airborne synthetic aperture radar observations of "spiral eddy" slick patterns in the Southern California Bight. *Journal of Geophysical Research: Oceans*, *115*(C5), C05010. https://doi.org/10.1029/2009jc005863

McWilliams, J. C. (2016). Submesoscale currents in the ocean. *Proceedings of the Royal Society A: Mathematical, Physical and Engineering Sciences*, *472*(2189), 20160117. https://doi.org/10.1098/rspa.2016.0117

Munk, W., Armi, L., Fischer, K., & Zachariasen, F. (2000). Spirals on the sea. *Proceedings of the Royal Society of London. Series A: Mathematical, Physical and Engineering Sciences*, *456*(1997), 1217–1280. https://doi.org/10.1098/rspa.2000.0560

Munk, W. H., & Cartwright, D. E. (1966). Tidal spectroscopy and prediction. *Philosophical Transactions of the Royal Society of London. Series A, Mathematical and Physical Sciences*, *259*(1105), 533–581.

Nam, S., & Send, U. (2013). Resonant diurnal oscillations and mean alongshore flows driven by sea/land breeze forcing in the coastal Southern California Bight. *Journal of Physical Oceanography*, *43*(3), 616–630. https://doi.org/10.1175/jpo-d-11-0148.1

Nencioli, F., Dong, C., Dickey, T., Washburn, L., & McWilliams, J. C. (2010). A vector geometry-based eddy detection algorithm and its application to a high-resolution numerical model product and high-frequency radar surface velocities in the Southern California Bight. *Journal of Atmospheric and Oceanic Technology*, *27*(3), 564–579. https://doi.org/10.1175/2009jtecho725.1

Ohlmann, C., White, P., Washburn, L., Emery, B., Terrill, E., & Otero, M. (2007). Interpretation of coastal HF radar-derived surface currents with high-resolution drifter data. *Journal of Atmospheric and Oceanic Technology*, *24*(4), 666–680. https://doi.org/10.1175/jtech1998.1

Oliver, E. C., Benthuysen, J. A., Bindoff, N. L., Hobday, A. J., Holbrook, N. J., Mundy, C. N., & Perkins-Kirkpatrick, S. E. (2017). The unprecedented 2015/16 Tasman Sea marine heatwave. *Nature Communications*, *8*(1), 16101. https://doi.org/10.1038/ncomms16101

Paduan, J. D., Kim, K. C., Cook, M. S., & Chavez, F. P. (2006). Calibration and validation of direction-finding high-frequency radar ocean surface current observations. *IEEE Journal of Oceanic Engineering*, *31*(4), 862–875. https://doi.org/10.1109/joe.2006.886195

Pennelly, C., & Myers, P. G. (2022). Tracking Irminger Rings' properties using a sub-mesoscale ocean model. *Progress in Oceanography*, *201*, 102735. https://doi.org/10.1016/j.pocean.2021.102735

Ray, R. D., & Egbert, G. D. (2004). The global S1 tide. *Journal of Physical Oceanography*, *34*(8), 1922–1935.

Schureman, P. (Ed.), (1958). *Manual of harmonic analysis and prediction of tides* (Vol. 98). US Government Printing Office.

Soh, H. S., & Kim, S. Y. (2018). Diagnostic characteristics of submesoscale coastal surface currents. *Journal of Geophysical Research: Oceans*, *123*(3), 1838–1859. https://doi.org/10.1002/2017jc013428

Stewart, R. H., & Joy, J. W. (1974). HF radio measurements of surface currents. *Deep Sea Research and Oceanographic Abstracts*, *21*(12), 1039–1049. https://doi.org/10.1016/0011-7471(74)90066-7

Thomas, L. N., Tandon, A., & Mahadevan, A. (2008). Submesoscale processes and dynamics.

Welch, P. (1967). The use of fast Fourier transform for the estimation of power spectra: A method based on time averaging over short, modified periodograms. *IEEE Transactions on Audio and Electroacoustics*, *15*(2), 70–73. https://doi.org/10.1109/tau.1967.1161901

Winant, C. D., & Dorman, C. E. (1997). Seasonal patterns of surface wind stress and heat flux over the Southern California Bight. *Journal of Geophysical Research: Oceans*, *102*(C3), 5641–5653. https://doi.org/10.1029/96jc02801

Zhang, T., Hoell, A., Perlwitz, J., Eischeid, J., Murray, D., Hoerling, M., & Hamill, T. M. (2019). Towards probabilistic multivariate ENSO monitoring. *Geophysical Research Letters*, *46*(17–18), 10532–10540. https://doi.org/10.1029/2019gl083946

Zhang, Y., Hu, C., Liu, Y., Weisberg, R. H., & Kourafalou, V. H. (2019). Submesoscale and mesoscale eddies in the Florida Straits: Observations from satellite ocean color measurements. *Geophysical Research Letters*, *46*(22), 13262–13270. https://doi.org/10.1029/2019gl083999

Zhao, D., Xu, Y., Zhang, X., & Huang, C. (2021). Global chlorophyll distribution induced by mesoscale eddies. *Remote Sensing of Environment*, *254*, 112245. https://doi.org/10.1016/j.rse.2020.112245